Energy & Environmental Science

Accepted Manuscript

ROYAL SOCIETY OF CHEMISTRY

www.rsc.org/ees

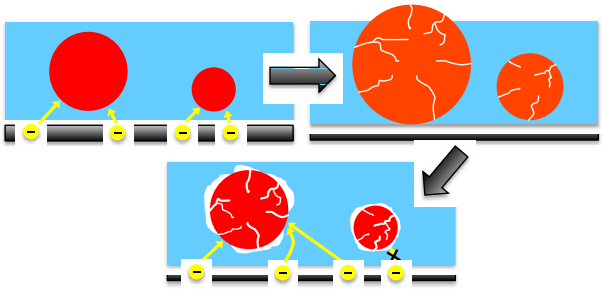

2D and 3D nanometer resolution imaging of Ge anodes during cycling show particle size-dependent fracturing and failure.

Journal Name

RSCPublishing

ARTICLE

In Situ Nanotomography and *Operando* Transmission X-ray Microscopy of Micron-sized Ge Particles

Cite this: DOI: 10.1039/xoxxoooooox

Received ooth January 2012,
Accepted ooth January 2012

DOI: 10.1039/xoxxoooooox

www.rsc.org/

J. Nelson Weker,[a] N. Liu [b], S. Misra,[a] J. C. Andrews,[a] Y. Cui,[c,d] and M. F. Toney[a]

To design an inexpensive, non-toxic, practical replacement to the internal combustion engine, significant advances in battery technology are required. Germanium anodes offer more than four times larger capacity than presently used graphite anodes. Yet large volume changes during operation severely limit their lifetime. To understand the origin, dynamics, and failure mechanisms of these and other electrode materials, it is essential to image batteries under operating conditions. Using transmission X-ray microscopy the morphology and electron density changes in Ge anode particles are tracked during operation. We observe significant size dependence on the cycling characteristics of Ge particles. Only Ge particles with diameters larger than a few microns display cracks during cycling. Small Ge particles experience volume expansion and cracking before their larger counterparts, but rapidly lose electrical contact. With *in situ* nanotomography, we demonstrate unambiguously for the first time the fracturing of alloying anode materials into completely unconnected pieces. Moreover, we show that the density changes due to lithiation are consistent with partial transformation into a $Li_{15}Ge_4$-like phase. Our results demonstrate the significant value in linking electrochemical performance studies with morphological evolution to understand failure mechanisms and encourage more systematic searches for a viable high capacity anode material.

Introduction

In the search for earth-abundant, high capacity materials for rechargeable batteries, alloying anodes such as silicon, germanium, and tin are excellent replacement candidates for the presently used graphite anode because of their substantially higher specific capacity.[1] Fully lithiated graphite stores one Li-ion per six carbon atoms through intercalation while, for example, fully lithiated germanium can theoretically store 4.4 Li-ions for every Ge atom. These large Li-ion storage capacities are extremely attractive and, at the same time, problematic: to accommodate such large Li concentrations, these anodes suffer enormous structural changes. As Li-ions are inserted and removed during battery cycling, these materials undergo up to 400% volume changes.[1-3] These sizable structural and volumetric changes are believed to be responsible for the rapid failure of these anodes after a few cycles. One possible failure mechanism is the fracturing and eventual pulverization of particles, which would render these fragments electronically isolated; therefore, they would no longer contribute to the total capacity of the electrode.[4-7] Understanding and mitigating the failure mechanisms of alloying anode materials is fundamental to utilizing the high storage capabilities of this class of electrode materials.

Due to its large, volumetric and specific capacity (8334 AhL^{-1} and 4200 $mAhg^{-1}$, respectively), silicon has drawn significant attention. Si is also inexpensive and earth abundant.[1, 2, 8, 9] However, Ge also has a sizable advantage in both volumetric and specific capacity (7366 AhL^{-1} and 1600 $mAhg^{-1}$, respectively) compared to graphite (833 AhL^{-1} and 372 $mAhg^{-1}$ respectively).[2, 10] Moreover, Ge is more electronically conductive and has higher lithium diffusivity than Si.[11, 12] Recent *in situ* transmission electron microscope (TEM) studies have shown that Ge nanoparticles are significantly more robust under cycling than similarly sized Si nanoparticles.[13, 14] Although the both materials undergo significant volume expansion (260% - 280%) during lithiation, Ge particles with diameters of 100s of nanometers do not fracture during lithiation, while Si fractures in particles with diameters >150 nm.[13]

In situ TEM studies have shown the morphological evolution of individual Ge nanostructures under constant potential.[13, 14] Recent demonstrations of the feasibility of *operando* TEM of liquid cells [15, 16] show the increasing interest and rapid developments in high resolution *operando* imaging of batteries. *Operando* hard x-ray transmission X-ray microscopy (TXM) complements TEM studies of single particles with its ability to image thick samples and large field of view, which can capture an image of a representative volume of the electrode.

High resolution, *operando* TXM studies have given important insight into cathode [17] and anode materials [18-20] in 2D (projection of electrode). Only a handful of *ex situ* 3D imaging studies have been performed on batteries with sub-micron resolution to visualize the pore structure in graphite anodes [21] and chemical distribution in nickel-nickel oxide cathode materials [22, 23] and nickel-sulfur compounds.[24] Volume expansion and fracturing have been visualized using *operando* X-ray tomography on tin oxide particles at a resolution of approximately 2 μm, allowing imaging of particles >5-10 μm.[25] Recently high resolution (~50 nm) *in situ* TXM has been demonstrated on tin anodes.[26] Since particles were imaged within a battery, but not during operation, the term *in situ* is used.

Here we report high resolution *in situ* and *operando* TXM of micron-sized Ge particles. Utilizing the penetration power of hard x-rays, batteries with total thicknesses in the millimeter range are studied with high spatial resolution (~30-50 nm) during typical battery operation (i.e. *operando*). We observe significant size dependencies to the cracking and cyclability of Ge particles. Only Ge particles with diameters larger than a few microns display cracks during cycling, and small Ge particles experience volume expansion and cracking before their larger counterparts, but rapidly lose electrical contact. By rotating a cell through a large angular range with respect to the X-ray beam, we visualize the *in situ* 3D structure of individual particles and calculate the density changes at key points along the cycle. We correlate the density changes to known Li-Ge alloys. This work represents the first direct demonstration of the physical and electronic disconnection of active electrode materials during cycling, which suggest possible paths to mitigating capacity fade in high capacity alloying anodes.

Results and discussion

Operando, 2D Microscopy

X-ray translucent batteries were constructed as described in the Supplementary Methods and imaged using TXM during constant current cycling. By utilizing an X-ray energy directly above the K-shell absorption edge of Ge (11.2 keV), there was a high contrast between the micron-size Ge particles and the other battery components. Absorption snapshots of a region containing Ge particles recorded during the first lithiation and ensuing delithiation are shown in Figure 1.

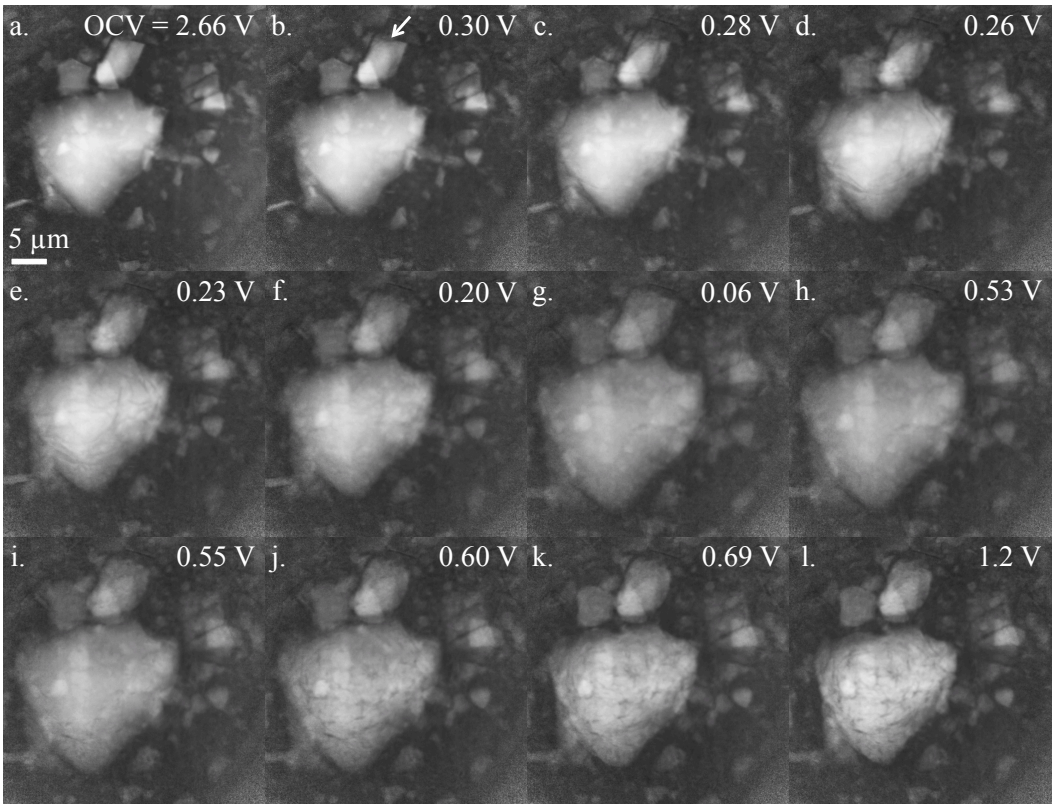

Figure 1. *In situ* TXM absorption snapshots of micron-size germanium particles during the first lithiation (a-g) and delithiation (h-l) cycle. In particles around 5 μm in diameter, crack formation is visible by 0.30 V during the lithiation cycle (arrow in (b)). Images were taking at 11.2 keV with a pixel size of 44 nm.

A total of five different 45 μm x 45 μm regions within the same cell were imaged concurrently. The voltages where the images were recorded are given in the top right corner of each panel and correspond to the electrochemical plot given in Figure S1

and the inset to Figure 2 (lithiation). Movies of the first and second cycle for all five regions are given in the supplemental material (M1 – M5). Because there is negligible absorption contribution from lithium and other cell components, any changes in brightness (or optical density) are linearly proportional to a change in particle electron density, by the Beer–Lambert law. Particles around 5 μm in diameter show visible crack formation by 0.30 V (Fig. 1b) during the lithiation cycle. At around 0.28 V (Fig. 1c) volume changes can be seen for the small particles and the largest particles show the beginning of fracturing. The cracks that form in the largest particle nucleate on the edges of the particle and travel inward. This suggests that a lithiation front travels from the shell of large particles towards the core creating stress, which results in fracturing.[4] As the cracking particles expand, the cracks fill in and most are no longer visible by 0.20 V (Fig. 1f). During delithiation (Fig. 1, h-l), as the cracked particles contract, the largest particles appear porous and do not return to their pristine shape or size (Compare Fig. 1 a,l).

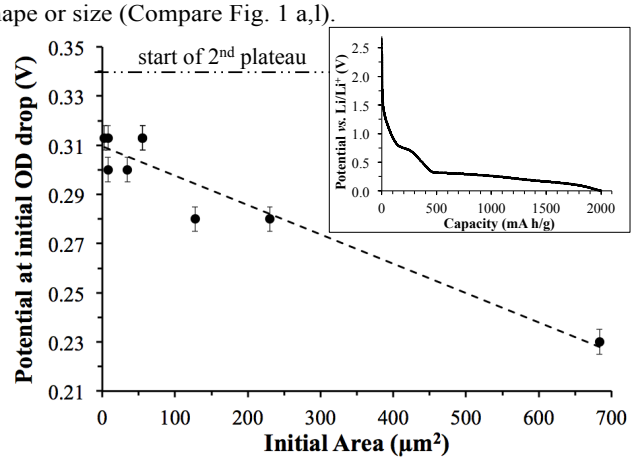

Figure 2. The initial potential at which a particle's average optical density (OD) begins to decrease in the first lithiation cycle is dependent on particle size before expansion. A linear guide to the data is included to show the trend only. The voltage at which the second lithiation potential starts is shown as a horizontal dashed line. Nine particles in total are plotted, however, two data points are indistinguishable on this plot at ~55 μm^2 initial area. The vertical error bars are based on the potential change between successive images. The capacity plot for the first lithiation cycle is displayed as an inset.

It is evident from many of the regions (Figure 1, M1 – M5), that there is a size dependence for the voltage at which volume expansion during lithiation is first detectable. The plot in Figure 2 shows that the initial potential at which a particle's average optical density (OD) begins to decrease due to lithiation is dependent on particle size before expansion. The average optical density (or absorption) was tracked rather than the change in particle area because it was less sensitive to noise. As particle size increases the barrier for lithiation induced volume expansion increases suggesting that a larger surface area to volume ratio results in faster lithiation. It is notable that all initial expansion potentials are appreciably below the start of the second voltage plateau (0.34 V), although the capacity indicates that at these potentials approximately one Li-ion has been inserted per germanium atom. Because no OD change is detected, this suggests that the Li-Ge alloys [27] formed above 0.31 V have densities similar to elemental germanium. Some of this lithium may also be inserting into the conductive carbon black matrix and reducing the native oxide layer.

If the initial potential at which a particle shows evidence of fracturing is monitored, a similar size dependent trend is observed; that is, larger particles begin to fracture at a lower potential than smaller particles. Particles begin to form cracks during their initial volume expansion. The smallest particle that was tracked, with an initial area of 2.9 μm^2, shows no crack formation during expansion. Assuming the cracks are not smaller than the imaging resolution of the microscope (~30 nm), this places the threshold of particle area, below which particles do not fracture, between 2.9 and 7.6 μm^2 (or a diameter of ~ 2 - 3 μm assuming spherical particles). This agrees with previous *in situ* TEM results which showed no fracturing in a Ge particle with a diameter of ~620 nm [13] and demonstrates that Ge particles can maintain a significantly larger particle size before fracturing than Si, which fractures at diameters above ~150 nm.[28] These results support the postulation by Liang *et al.*[13] that the isotropic volume expansion of germanium particles makes them more robust under cycle than silicon particles which have been shown to expand anisotropically.[5]

During the delithation cycle, there is no evidence of a size dependence for the potential at which initial particle contraction is detected. This can be explained by the increased porosity of the large particles due to fracturing during lithiation. The fracturing during lithiation and the increased porosity from lithium extraction increase the surface area to volume ratio of the large particles such that they delithiate as if they were agglomerations of smaller particles.

The same five regions were also imaged during the second lithiation and delithiation cycle (Figure 3, M1 – M5). Outlines of the three largest particles at the start of the second lithiation (Fig. 3a) have been duplicated onto the same particles after lithiation (Fig. 3f). It is evident that only the largest particle in this region expands and contracts during the second cycle. This shows that this is the only particle in the region participating in the second cycle and suggests that the remaining particles have lost electrical contact with the current collector. This observation of the loss of electrical contact during electrochemical cycling is similar to results seen in Si nanoparticles using *in situ* TEM. Silicon nanoparticles embedded in a carbon matrix led to fracturing of the carbon fiber during lithiation,[29] and Si nanoparticles within a silicon-conductive polymer composite sustained good electrical contact when compared to the conventional electrode preparation method.[30] Figure 4 is a plot of the fraction of particles that are actively participating (black) and those that are not (gray and striped) in the second cycle against the initial area of each of the nine particles from Fig. 2. Less than a third of the nine particles tracked are active in the second cycle. Although the total number of particles is relatively low, a strong particle size dependence for the second cycle participation is clear. Only the largest particles show evidence of volume changes.

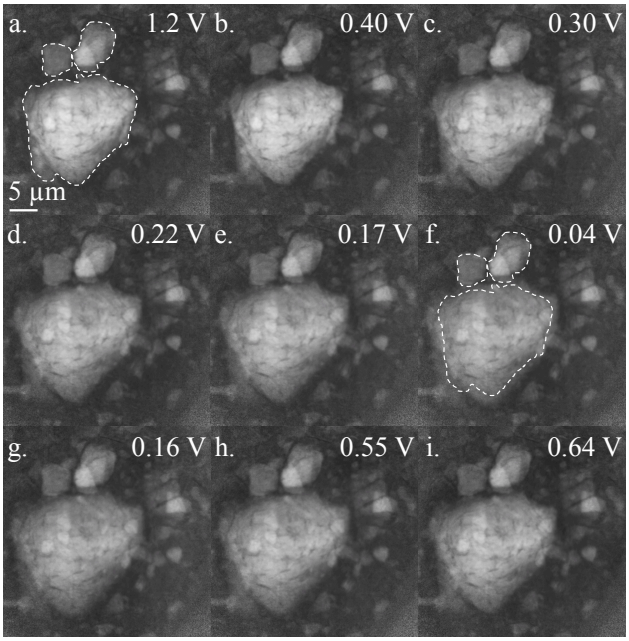

Figure 3. *In situ* TXM absorption snapshots of micron-size germanium particles during the second lithiation (a-f) and delithiation (g-i) cycles. The voltages at which the images were recorded are given in the top right corner of each panel. During the second lithiation and delithiation cycles, only the largest particle in this region expands. Outlines of the three largest particles at the start of the second lithiation (a) have been duplicated onto the same particles after lithiation (f) to show that only the largest particle undergoes a visible expansion.

This size dependence is perhaps initially counterintuitive since the larger particles tend to fracture and break apart, which could cause the fractured pieces to lose physical contact with the current collector.[4] However, the size dependence can be explained by considering the contact area that particles of a particular size have with the surrounding conductive carbon and binder matrix. Since the larger particles have larger surface areas, they tend to have more points of contact between the particles and the carbon/binder matrix. During lithiation, the particles expand pushing the carbon/binder matrix outwards (Figure 5). When the current is reversed and the particles begin to delithiate and contract, the conductive matrix does not necessarily shrink back to fill the space created by the contracting particles (Fig. 5c). It appears that most of the physical connections between the particles have with the carbon/binder matrix are severed during the delithiation cycle. In fact, the solid gray bars in Fig. 4 show these particles that did not participate in the end of the first delithiation cycle: between 0.55 V and 0.6 V these particles ceased to contract in volume. This indicates the point in the first delithiation cycle when these particles' physical connections to the conducting matrix were lost (M1, 4, and 5). This permanent deformation of the carbon/binder matrix during the first lithiation cycle is consistent with *operando* micro-tomography results by Ebner *et al.* on SnO anodes.[25]

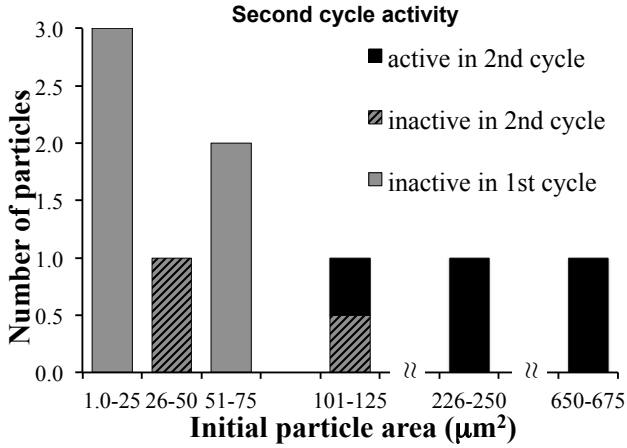

Figure 4. Plot of the fraction of particles which actively participate in the second cycle (black), become inactive before the end of the first cycle (gray), and do not actively participate in the second cycle (striped) against the initial area of the particles. The bar representing a single particle shaded both black and gray with stripes designates that only portion of the particle exhibits a volume change.

Because of their relatively small volumes, the electronically disconnected particles account for only about a 10% loss in capacity after the first cycle (assuming large particles fully lithiate, which is not completely correct). This can account for 25% or more of the total capacity loss in that cycle (Figure S1). A newly developed self healing polymer binder may help to counter this capacity loss by allowing small to medium micron-sized Ge particles to remain electronically connected after the first cycle.[31]

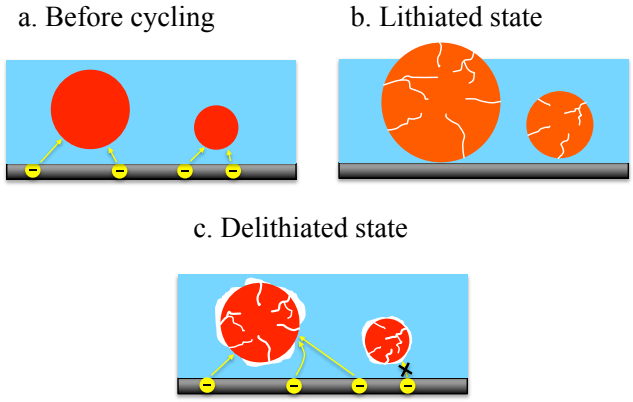

Figure 5. Schematic of the irreversible deformation of the carbon/polymer binder matrix (blue) due to the large Ge (red/orange) volume changes during the first cycle which results in smaller particles becoming physically disconnected from the conductive matrix rendering them inactive in subsequent cycles.

Finally, it is worth discussing the unique observations seen in the largest particle imaged in the *operando* TXM study. The movie M3 shows a preferential direction of fracturing during the first lithiation cycle. The initial cracks begin on only one side of the particle (right side) and then travel inward as additional cracks form around the outside of the particle. This anisotropic cracking is likely due to an uneven distribution of electronic pathways connecting the particle to the current collector. No other particle shows a preferred direction of crack formation or volume expansion. After the first

expansion/contraction cycle, the particle no longer exhibits a preferential lithiation direction suggesting that the points of contact with the conductive carbon have been rearranged by the volume changes.

A second observation particular to the largest particle is shown in Figure S2. *In situ* TXM absorption snapshots of the largest particle observed after the first lithation cycle (left) and after the second lithation cycle (right) indicate that the volume expansion during the second lithiation cycle is significantly greater. This can be explained by the increased porosity of the particle after the first cycle, which increased the Li-ion diffusion into the center of the particle.[32, 33] This is direct evidence that the cycling rate (C/5) was likely too quick to lithiate the largest particle completely in the first cycle and agrees with previous results.[34] The increased expansion in the second cycle contributes to a capacity gain, which offsets the capacity losses due to the electrical disconnection of the smaller particles.

In Situ Tomography

An X-ray transparent battery constructed identically to the one imaged in the previous section was imaged *in situ* using 3D tomographic TXM. Particles in three different regions were imaged before cycling, after the first lithiation cycle, and after the first delithiation cycle. The first cycle electrochemistry for this cell is given in Figure S3. Volume renderings with corresponding cross-sections through the volume of Ge particles is given in Figure 5 from one of the regions before cycling (a, d), after the first lithiation cycle (b, e), and after the first delithiation cycle (c, f). Arrows show the location of large cracks formed during the lithiation cycle (Fig. 5b) that fractured the largest particle during the delithiation cycle (Fig. 5c). This is the first unambiguous demonstration of an alloying anode material fracturing into completely isolated pieces during the delithiation cycle. In the supplemental material, Figures S4 and S5 are the equivalent figures for the other two regions.

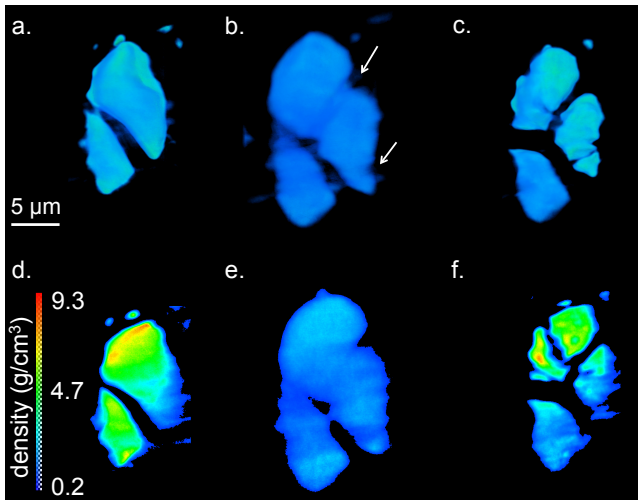

Figure 5. Volume renderings (above) with corresponding cross-sections through the volume (below) from *in situ* tomographic imaging of Ge particles (a, d) before cycling, (b, e) after the first lithiation cycle, and (c, f) after the first delithiation cycle. Arrows indicate large cracks formed during the lithiation cycle (b) that fracture the largest particle during delithiation (c). Data were smoothed with a median filter for display only. The scale and color bars correspond to the volume renderings and 2D slices.

The density changes in the Ge particles were tracked by selecting a 2.2 µm x 2.2 µm x 2.2 µm subvolume entirely within a Ge particle (Figure S6). The average Ge density of the subvolume in this region is plotted in Figure 6. An explanation of how the Ge density is calibrated is given in the Methods Section. The peak density in this region, determined by Gaussian fitting, is 5.32 g/cm^{-3} before cycling, 1.68 g/cm^{-3} after lithation, and 5.12 g/cm^{-3} after delithiation. This corresponds to a ~320% drop in density after lithiation but nearly a complete recovery of the density after delithiation. However, from the density plots it is clear that the delithiation curve is significantly broader and shifted to lower density although some voxels return to their original density. The literature value for the density of $Li_{15}Ge_4$ is 2.13 g/cm^{-3}.[35] If we consider just the density contribution from Ge by removing the mass of the Li-ions, the density of the Ge contribution in $Li_{15}Ge_4$ is 1.57 g/cm^{-3}. This is consistent with the particle partially in the $Li_{15}Ge_4$ state.

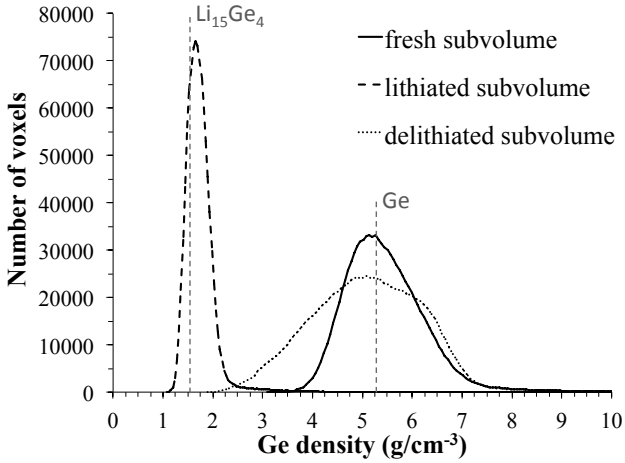

Figure 6. Plot of the Ge density histogram within a 2.2 µm x 2.2 µm x 2.2 µm subvolume taken from entirely within the largest Ge particle in Fig. 5. The Ge densities for Ge and $Li_{15}Ge_4$ are displayed as vertical dashed lines. After lithiation the peak shifts to lower density, corresponding to a ~320% drop in density. The peak falls just shy of the Ge density expected for pure $Li_{15}Ge_4$. After delithiation the peak center returns nearly to the peak position before cycling, but it has a broad tail towards lower density indicating that many voxels are not entirely delithiated.

Across the three regions studied, the Ge density, dropped to an average of 1.76 g/cm^{-3} after lithiation or a ~315% drop in density. It returned to 5.09 g/cm^{-3} after delithation. The change during lithiation is well below the theoretical value (370%),[11] but is larger than the changes observed previously in nano-sized Ge particles (~260%) with *in situ* TEM.[13] The percent change in density from the pristine state varies significantly for both lithiation and delithiation in the three regions with standard deviations of 45% and 55%, respectively. In the future, more particles need to be studied using *in situ* tomographic imaging to increase the statistics and extract any possible trends.

Conclusions

Using high resolution TXM, we have imaged micron-sized Ge particles *operando* to track morphology and electron density changes in 2D. By tracking a number of particles of different

sizes, we have shown that the smallest particles change volume first (higher potential) during the first lithiation cycle. This size dependence is not seen in the delithiation cycle or during the second lithiation cycle. After the first lithiation, fracturing in the largest particles increases the surface area to volume ratio, allowing the large particles to (de)lithiate in a similar fashion as smaller particles. We have determined that particles with areas below 2.9 μm^2 (or a diameter of ~2 μm, assuming spherical particles) do not fracture during cycling. Germanium benefits from a significantly larger particle volume before fracturing occurs, than its silicon counterpart. Finally, we demonstrated a strong size dependence for active participation in the second (de)lithiation cycle: only the largest third of the particles participated. Most particles lost physical connection with the conductive carbon/binder matrix by the end of the first delithiation cycle and were no longer electronically connected to the current collector. This partly explains the reason for capacity fading in Ge anodes. Due to their larger surface area, larger particles tend to have more contact points to the conductive carbon making the particles more likely to maintain electronic connection to the current collector.

With *in situ* nanotomography, we have confirmed that the largest Ge particles can break apart during the first delithiation cycle. This is the first unambiguous demonstration of fracturing of alloying anode materials into completely unconnected pieces. Moreover, density changes in micron-size Ge particles have been calculated to drop to an average of 1.76 g/cm^{-3} after lithiation (consistent with $Li_{15}Ge_4$).

Our 2D *operando* and 3D *in situ* imaging results support the development of a large (>15 μm diameter) porous Ge particle architecture [32, 33] to ensure more complete (de)lithiation of particles and to maintain electrical contact with the current collector. In addition, the results suggest that the use of specifically engineered binders such as self-healing polymers[31] or conductive polymer composites[30] may be essential in preventing capacity loss from electronic disconnection of particles after the first cycle. The high penetration power and large field of view of *operando* nanometer resolution TXM enable the study of a number of different permutations of Ge and other anode and cathode particle architectures and advanced binders. By linking electrochemical performance studies with morphological evolution the search for a viable high capacity anode material becomes more systematic.

Acknowledgements

Portions of this research were carried out at the Stanford Synchrotron Radiation Lightsource, a national user facility operated by Stanford University on behalf of the U.S. Department of Energy, Office of Basic Energy Sciences.

Notes and references

[c] Stanford Synchrotron Radiation Lightsource, SLAC National Accelerator Laboratory, Menlo Park, CA, USA.

[b] Department of Chemistry, Stanford University, Stanford, CA, USA.

[c] Department of Materials Science and Engineering, Stanford University, Stanford, CA, USA.

[d] Stanford Institute for Materials and Energy Sciences, SLAC National Accelerator Laboratory, Menlo Park, CA, USA

Electronic Supplementary Information (ESI) available: [Experimental section, schematic of proposed electrode deformation, electrochemistry of *operando* cell, evidence of additional capacity in second cycle, electrochemistry of *operando* cell, electrochemistry of *in situ* 3D cell, volume renderings and cross-sections from two additional regions, subvolumes uses in normalization of 3D data, five movies of Ge particles during cycling]. See DOI: 10.1039/b000000x/

1. M. T. McDowell, S. W. Lee, W. D. Nix and Y. Cui, *Advanced Materials*, 2013, 25, 4966-4985.
2. D. Larcher, S. Beattie, M. Morcrette, K. Edstrom, J.-C. Jumas and J.-M. Tarascon, *Journal of Materials Chemistry*, 2007, 17, 3759-3772.
3. M. N. Obrovac, L. Christensen, D. B. Le and J. R. Dahn, *Journal of The Electrochemical Society*, 2007, 154, A849-A855.
4. R. A. Huggins and W. D. Nix, *Ionics*, 2000, 6, 57-63.
5. X. H. Liu, H. Zheng, L. Zhong, S. Huang, K. Karki, L. Q. Zhang, Y. Liu, A. Kushima, W. T. Liang, J. W. Wang, J. H. Cho, E. Epstein, S. A. Dayeh, S. T. Picraux, T. Zhu, J. Li, J. P. Sullivan, J. Cumings, C. Wang, S. X. Mao, Z. Z. Ye, S. Zhang and J. Y. Huang, *Nano Letters*, 2011, 11, 3312-3318.
6. N. Liu, H. Wu, M. T. McDowell, Y. Yao, C. Wang and Y. Cui, *Nano Letters*, 2012, 12, 3315-3321.
7. L. Y. Beaulieu, K. W. Eberman, R. L. Turner, L. J. Krause and J. R. Dahn, *Electrochemical and Solid-State Letters*, 2001, 4, A137-A140.
8. B. Key, R. Bhattacharyya, M. Morcrette, V. Seznéc, J.-M. Tarascon and C. P. Grey, *Journal of the American Chemical Society*, 2009, 131, 9239-9249.
9. C. K. Chan, H. Peng, G. Liu, K. McIlwrath, X. F. Zhang, R. A. Huggins and Y. Cui, *Nature Nano*, 2008, 3, 31-35.
10. J. Chen, *Materials*, 2013, 6, 156-183.
11. C. K. Chan, X. F. Zhang and Y. Cui, *Nano Letters*, 2007, 8, 307-309.
12. J. Graetz, C. C. Ahn, R. Yazami and B. Fultz, *Journal of The Electrochemical Society*, 2004, 151, A698-A702.
13. W. Liang, H. Yang, F. Fan, Y. Liu, X. H. Liu, J. Y. Huang, T. Zhu and S. Zhang, *ACS nano*, 2013, 7, 3427-3433.
14. X. H. Liu, S. Huang, S. T. Picraux, J. Li, T. Zhu and J. Y. Huang, *Nano Letters*, 2011, 11, 3991-3997.
15. M. Gu, L. R. Parent, B. L. Mehdi, R. R. Unocic, M. T. McDowell, R. L. Sacci, W. Xu, J. G. Connell, P. Xu, P. Abellan, X. Chen, Y. Zhang, D. E. Perea, J. E. Evans, L. J. Lauhon, J.-G. Zhang, J. Liu, N. D. Browning, Y. Cui, I. Arslan and C.-M. Wang, *Nano Letters*, 2013, 13, 6106-6112.
16. M. E. Holtz, Y. Yu, D. Gunceler, J. Gao, R. Sundararaman, K. A. Schwarz, T. A. Arias, H. D. Abruña and D. A. Muller, *Nano Letters*, 2014, 14, 1453-1459.
17. J. Wang, Y.-c. K. Chen-Wiegart and J. Wang, *Chemical Communications*, 2013, 49, 6480-6482.
18. S.-C. Chao, Y.-F. Song, C.-C. Wang, H.-S. Sheu, H.-C. Wu and N.-L. Wu, *The Journal of Physical Chemistry C*, 2011, 115, 22040-22047.
19. S.-C. Chao, Y.-C. Yen, Y.-F. Song, Y.-M. Chen, H.-C. Wu and N.-L. Wu, *Electrochemistry Communications*, 2010, 12, 234-237.
20. S.-C. Chao, Y.-C. Yen, Y.-F. Song, H.-S. Sheu, H.-C. Wu and N.-L. Wu, *Journal of Electrochemical Society*, 2011, 158, A1335-A1339.
21. P. R. Shearing, L. E. Howard, P. S. Jørgensen, N. P. Brandon and S. J. Harris, *Electrochemistry Communications*, 2010, 12, 374-377.
22. F. Meirer, J. Cabana, Y. Liu, A. Mehta, J. C. Andrews and P. Pianetta, *Journal of synchrotron radiation*, 2011, 18, 773-781.
23. G. J. Nelson, W. M. Harris, J. R. Izzo, K. N. Grew, W. K. S. Chiu, Y. S. Chu, J. Yi, J. C. Andrews, Y. Liu and P. Pianetta, *Applied Physics Letters*, 2011, 98, -.
24. W. M. Harris, G. J. Nelson, A. M. Kiss, J. R. Izzo, Y. Liu, M. Liu, S. Wang, Y. S. Chu and W. K. S. Chiu, *Nanoscale*, 2012, 4, 1557-1560.
25. M. Ebner, F. Marone, M. Stampanoni and V. Wood, *Science (New York, N.Y.)*, 2013, DOI: 10.1126/science.1241882.
26. J. Wang, Y.-c. K. Chen-Wiegart and J. Wang, *Angewandte Chemie International Edition*, 2014, DOI: 10.1002/anie.201310402, n/a-n/a.

27. L. Baggetto, E. J. M. Hensen and P. H. L. Notten, *Electrochimica Acta*, 2010, 55, 7074-7079.
28. X. H. Liu, L. Zhong, S. Huang, S. X. Mao, T. Zhu and J. Y. Huang, *ACS nano*, 2012, 6, 1522-1531.
29. M. Gu, Y. Li, X. Li, S. Hu, X. Zhang, W. Xu, S. Thevuthasan, D. R. Baer, J.-G. Zhang, J. Liu and C. Wang, *ACS nano*, 2012, 6, 8439-8447.
30. M. Gu, X.-C. Xiao, G. Liu, S. Thevuthasan, D. R. Baer, J.-G. Zhang, J. Liu, N. D. Browning and C.-M. Wang, *Sci. Rep.*, 2014, 4.
31. C. Wang, H. Wu, Z. Chen, M. T. McDowell, Y. Cui and Z. Bao, *Nature Chemistry*, 2013, 5, 1042-1048.
32. L. C. Yang, Q. S. Gao, L. Li, Y. Tang and Y. P. Wu, *Electrochemistry Communications*, 2010, 12, 418-421.
33. M.-H. Park, K. Kim, J. Kim and J. Cho, *Advanced Materials*, 2010, 22, 415-418.
34. Y. J. Cho, H. S. Im, H. S. Kim, Y. Myung, S. H. Back, Y. R. Lim, C. S. Jung, D. M. Jang, J. Park, E. H. Cha, W. I. Cho, F. Shojaei and H. S. Kang, *ACS nano*, 2013, 7, 9075-9084.
35. Q. Johnson, G. S. Smith and D. Wood, *Acta Crystallographica*, 1965, 18, 131-132.